Dalton Transactions

ROYAL SOCIETY OF CHEMISTRY

PAPER

View Article Online
View Journal | View Issue

Check for updates

Cite this: *Dalton Trans.*, 2025, **54**, 17211

A tetradentate benzannulated P^N^N^P ligand and its Fe(II) complex: synthesis, characterization, and electrocatalytic hydrogen evolution

Baldeep K. Sidhu, Amelia Kacperkiewicz, Jason D. Braun and David E. Herbert *

Received 13th September 2025,
Accepted 24th October 2025

DOI: 10.1039/d5dt02202a

rsc.li/dalton

Iron complexes supported by phosphine and pyridine-based ligands are widely seen as efficient molecular catalysts for catalytic transformations, but examples of these complexes as molecular electrocatalysts for the hydrogen evolution reaction (HER) are limited. In this work, we present a ligand design based on a 6,6′-fused dimer of a 2,4-substituted (phosphino)phenanthridine (benzo[*c*]quinoline). Starting from the monomeric P^N precursor, we show how the P^N^N^P dimer can be selectively formed and report the synthesis and characterization of an Fe(II) complex of this unique scaffold. We demonstrate the potential of such frameworks in the electrocatalytic reduction of Brønsted acids in acetonitrile solution.

Open Access Article. Published on 30 October 2025. Downloaded on 5/16/2026 7:15:46 PM. This article is licensed under a Creative Commons Attribution 3.0 Unported Licence.

Introduction

Hybrid P^N ligands containing both soft phosphorus and hard nitrogen donors are widespread in organometallic chemistry, finding utility in catalytic hydrogenation,[1,2] asymmetric transformations,[3] cross-coupling reactions,[4,5] and more. Higher denticity analogs are also gaining in popularity. Examples include tridentate P^N^P 'pincer' ligands[6] and tetradentate P_2N_2 ligands based on salen[7] or more flexible[8–10] scaffolds (Fig. 1). The latter category is dominated by 1,5-diaza-3,7-diphosphacyclooctanes (Fig. 1a), first popularized for their use in bio-inspired electrocatalysis[10] and now expanding into areas including acceptorless dehydrogenation[11] and cross-coupling.[12] Coordination complexes of 1,5-diaza-3,7-diphosphacyclooctanes largely present κ^2-diphosphine coordination, with the P_2N_2 ligand binding solely through the phosphine donor sites. This allows for the uncoordinated tertiary amino groups to act as biomimetic proton relays in electrochemical hydrogen evolution reactivity (HER), similar to the proposed role of the bridgehead nitrogen present in the bridging dithiolate of [FeFe]-hydrogenase.[13] Pendant bases are not, however, required for efficient electrocatalysis. Monometallic 3d metal complexes with polypyridine and/or phosphine ligands also efficiently catalyze the reduction of protons to H_2.[14] Porphyrins,[15] amine-bis(phenolates),[16] fluorinated diglyoxime ligands,[17] and multidentate polypyridyl frameworks[18–20] are all capable of supporting HER-active Fe centres.

Our longstanding interest in ligands bearing benzannulated N-heterocyclic donors based on phenanthridine (benzo[*c*]quinoline) moieties[21] has recently extended to bipyridine analogs such as 6,6′-biphenanthridine (biphe)[22] and its planar, doubly-fused congener 6,6′,7,7′-biphenanthridine (*p*-biphe).[23] These motifs combine the benzannulation seen in 2,2′-biquinoline with that of 1,1′-biisoquinoline. In this work, we present a strategy for the synthesis of a substituted phosphine-decorated 6,6′-biphenanthridine, starting from its monomeric precursor.[24] We strategized that the large π-extended biphenan-

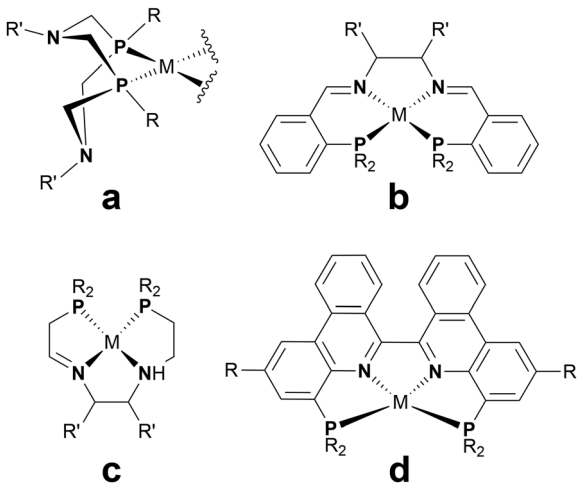

Fig. 1 Selected examples of P_2N_2 ligands: (a) flexible, macrocyclic P^P chelating diphosphine ligands with pendant amines;[10] (b) rigid salen-type P^N^N^P chelates;[7] (c) flexible P^N^N^P scaffolds;[8,9] (d) the benzannulated tetradentate P^N^N^P framework reported in this work.

Department of Chemistry and the Manitoba Institute for Materials, University of Manitoba, 144 Dysart Road, Winnipeg, Manitoba, R3T 2N2, Canada.
E-mail: david.herbert@umanitoba.ca

Open Access Article. Published on 30 October 2025. Downloaded on 5/16/2026 7:15:46 PM.
This article is licensed under a Creative Commons Attribution 3.0 Unported Licence.

thridine core might stabilize a reduced state and lower the overpotential for HER.[25] We use this tetradentate P^N^N^P ligand, with two phosphine donor arms and two phenanthridine donor arms, to form a six-coordinate Fe(II) coordination complex bearing two axial acetonitrile units. The utility of this species in electrocatalytic HER activity is described.

Results and discussion

We previously described the synthesis of biphe *via* nickel(0)-mediated homocoupling of (6-trifluoromethanesulfonato)phenanthridine.[22] Biphe can chelate transition metal ions *via* κ^2-N^N coordination. To augment the binding ability of biphe we envisioned accessing a phosphine-substituted derivative capable of tetradentate P^N^N^P coordination *via* reductive dimerization of (4-diphenylphosphino-2-methyl)phenanthridine (**L**, Fig. 2). We have reported the preparation of the parent (4-diphenylphosphino)phenanthridine[24] but find in general installing a substituent at the 2-position smooths the preparation of the (4-bromo)phenanthridine precursor needed for preparation of the phosphine.[26] (4-Diphenylphosphino-2-methyl)phenanthridine has been used to support orange emissive halide-bridged Cu(I) dimers,[27,28] tetrahedral and trigonal bipyramidal Fe(II) as well as pseudo-octahedral Fe(II) and Ru(II) complexes,[29] along with a Ru(II)-based catalyst useful for acceptorless dehydrogenative couplings[30–32] and a unique tandem hydrogen-borrowing dehydrogenative coupling/hydrodefluorination system.[33]

Phenanthridine can be electrochemically hydrogenated to dihydrophenanthridine using an applied potential in the presence of weak Brønsted acids.[34,35] Accordingly, we reasoned that with a strong enough reductant, we might be able to form a radical at the 6-position of **L** (see Fig. 2a for the IUPAC numbering scheme for phenanthridines) and facilitate reductive dimerization. The LUMOs of phenanthridines, in general, are localized at the π*(C═N) sub-unit.[21] Should dimerization occur, addition of water to the reaction mixture was anticipated to lead to the formation of 5,5′,6,6′-tetrahydro-6,6′-bis((4-diphenylphosphino-2-methyl)phenanthridinyl) (**[L^L]-2H$_2$**) which might then be oxidized to **L^L**. In our first successful attempt, **L** was reacted with an excess of sodium-mercury amalgam (5% Na in Hg) at 110 °C in toluene for 48 h. The reaction mixture initially turned from yellow to dark brown, then gradually to dark blue, and finally to olive-green. These vibrant colours are consistent with the expected radical mechanism. Quenching the reaction mixture with excess water, however, largely produced **L^L** with no evidence of **[L^L]-2H$_2$**. $^{31}P\{^1H\}$ NMR spectroscopic analysis showed 44% conversion to **L^L**, minor amounts of the hydrogenated monomer 5,6-dihydro(4-diphenylphosphino-2-methyl)phenanthridine (**L-H$_2$**), 5,6-dihydro-bis((4-diphenylphosphino-2-methyl)phenanthridyl) (**[L^L]-H$_2$**), and some unreacted starting material (Fig. S1). In searching for optimal conditions for the formation of **L^L**, we varied the nature and equivalents of the reductant, reaction duration, and amount of water added to quench the reaction (Table S1). In the end, heating **L** in the presence of two equivalents of elemental sodium in refluxing toluene over 4 d yielded appreciable amounts of the target compound (Fig. 2a). The results of these trials led us to propose an alternate mechanism wherein direct elimination of sodium hydride from the dimerized disodium salt intermediate at high temperature directly forms **L^L** (Fig. 2b).[36]

The formation of the hydrogenated monomer **L-H$_2$** and partially hydrogenated **[L^L]-H$_2$** likely arises from the presence of NaH in the reaction mixture, which can react with water to

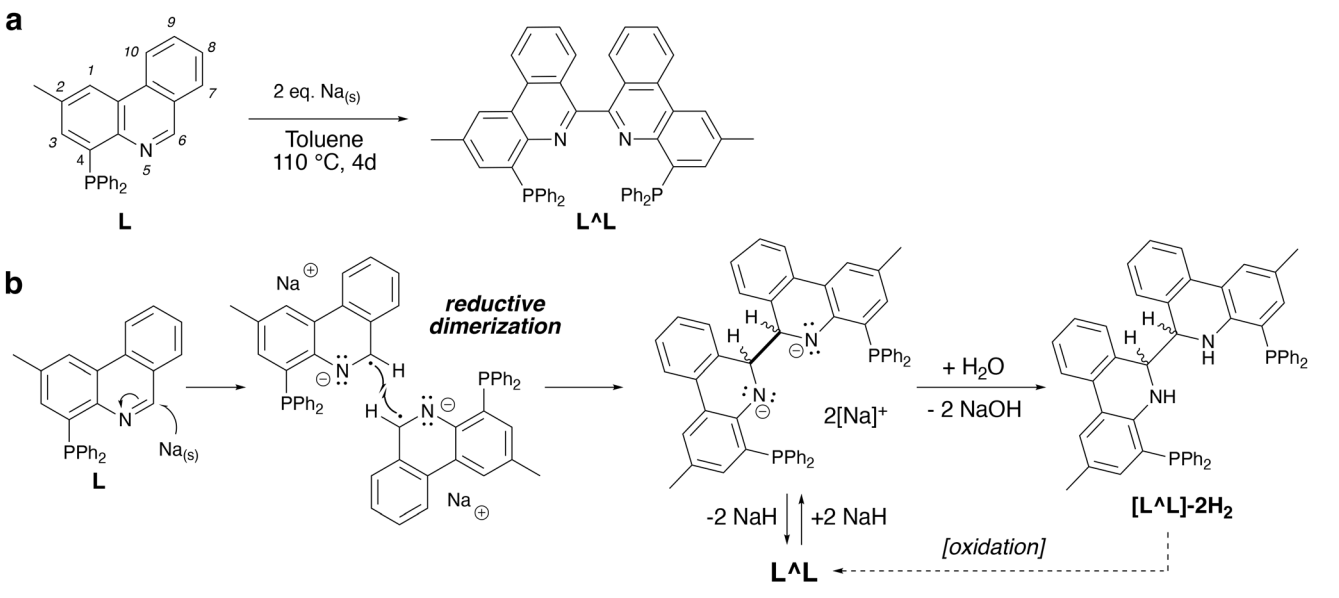

Fig. 2 (a) Optimized synthetic route to L^L (IUPAC numbering scheme for phenanthridines is shown in italics) and (b) the proposed mechanism for formation of L^L and [L^L]-2H$_2$ through addition of water to the crude reaction mixture.

 This journal is © The Royal Society of Chemistry 2025

Open Access Article. Published on 30 October 2025. Downloaded on 5/16/2026 7:15:46 PM.
This article is licensed under a Creative Commons Attribution 3.0 Unported Licence.

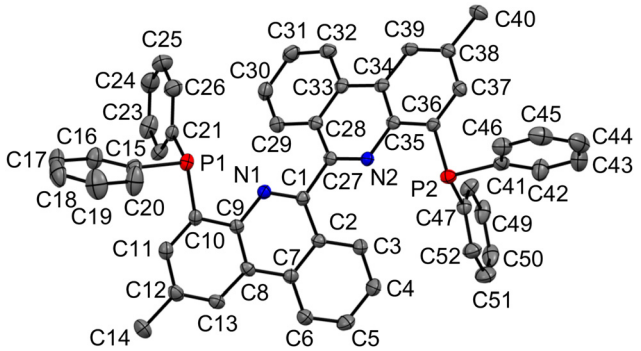

Fig. 3 Solid state structure of **L^L** obtained *via* single crystal XRD, with thermal ellipsoids shown at 50% probability level and hydrogen atoms omitted for clarity. Selected bond distances (Å) and angles (°): C(1)–N(1) 1.303(4), C(1)–C(2) 1.452(4), C(2)–C(7) 1.409(4), C(7)–C(8) 1.448(4), C(8)–C(9) 1.406(4), C(9)–N(1) 1.381(4), C(10)–P(1) 1.836(3), C(1)–C(27) 1.500(4), C(27)–N(2) 1.306(4), C(27)–C(28) 1.447(4), C(28)–C(33) 1.409(4), C(33)–C(34) 1.443(4), C(34)–C(35) 1.407(4), C(35)–N(2) 1.385(4), C(36)–P(2) 1.831(3), N(1)–C(1)–C(27) 115.9(2), C(1)–N(1)–C(9) 119.4(2), N(1)–C(1)–C(2) 123.1(3), C(1)–C(27)–N(2) 115.9(2), C(27)–N(2)–C(35) 118.9(2), N(2)–C(27)–C(28) 123.7(3), N(1)–C(1)–C(27)–N(2) 122.23.

produce H_2 gas or directly with **L** in the presence of water as a proton source.[37] Indeed, higher amounts of **L-H$_2$** and **[L^L]-H$_2$** were observed when excess water was used to quench the unreacted sodium. Elimination of sodium hydride to make **L^L** is more favourable than formation of **[L^L]-2H$_2$** as NaH elimination restores aromaticity, which provides a driving force for the elimination. Accordingly, we hypothesized that filtering the reaction mixture before adding water would separate insoluble, solid NaH and prevent hydrogenation of the unreacted monomer or the dimer (Run 8, Table S1). Gratifyingly, adding a filtration step avoided all formation of hydrogenated side products. Our optimal workup excludes the water addition step altogether: the precipitate formed in the reaction mixture (presumed to be NaH) and any unreacted Na are separated by filtration and quenched with water separately, with no water added to the filtrate. In this way, **L^L** can be isolated in 70% yield as a light yellow solid following washing with minimal amounts of toluene to remove unreacted starting material.

^{1}H NMR analysis showed the two phenanthridine units to be chemically equivalent, with loss of the diagnostic imine proton at the 6-position which typically appears up as a downfield singlet at $\delta > 9$ ppm. Compared with the monomer **L**, signals of the two aromatic hydrogen nuclei at the 7- and 8-positions are significantly shifted upfield. Single crystals of

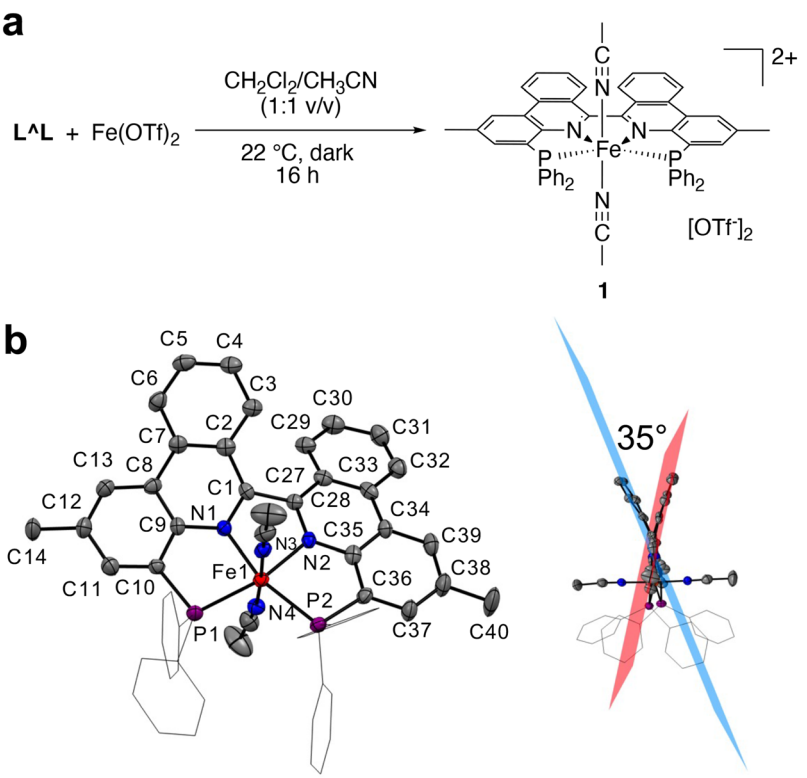

Fig. 4 (a) Synthesis of **1** and (b) its solid-state structure with thermal ellipsoids shown at 50% probability levels. Hydrogen atoms, counterion molecules, and solvent molecules have been omitted, and phenyl substituents drawn as a wireframe for clarity. Selected bond distances (Å) and angles (°): Fe(1)–N(1) 1.946(8), Fe(1)–N(2) 1.963(8), Fe(1)–N(3) 1.911(8), Fe(1)–N(4) 1.920(8), Fe(1)–P(1) 2.249(3), Fe(1)–P(2) 2.241(3), C(1)–N(1) 1.34(1), C(1)–C(27) 1.48(1), C(27)–N(2) 1.32(1), N(1)–Fe(1)–N(2) 80.6(3), N(1)–Fe(1)–N(3) 91.1(3), N(1)–Fe(1)–N(4) 86.5(3), N(1)–Fe(1)–P(1) 85.5(2), N(1)–Fe(1)–P(2) 164.9(2), N(2)–Fe(1)–N(3) 88.5(3), N(2)–Fe(1)–N(4) 91.7(3), N(1)–C(1)–C(27) 111.0(7), C(1)–N(1)–C(9) 120.3(8), N(1)–C(1)–C(2) 120.9(8), C(1)–C(27)–N(2) 113.5(7), C(27)–N(2)–C(35) 122.4(8), N(2)–C(27)–C(28) 120.2(8), N(1)–C(1)–C(27)–N(2) 111.0(7).

Open Access Article. Published on 30 October 2025. Downloaded on 5/16/2026 7:15:46 PM.
This article is licensed under a Creative Commons Attribution 3.0 Unported Licence.

quality suitable for X-ray diffraction experiments could be obtained by layering pentane over a concentrated dichloromethane solution of **L^L** (Fig. 3). The bond distances and bond angles in the dimer are generally similar to the P^N precursor itself.[24] The newly formed C1–C27 bond has a bond distance of 1.500(4) Å, typical of a N═C–C═N sub-unit. The C1–N1 [1.303(4) Å] and C27–N2 [1.306(4) Å] distances are consistent with the C═N character, in line with the 'imine-bridged biphenyl' character of phenanthridines in general.[21] These distances, and the C9–N1–C1 [119.4(3)°] and C27–N2–C35 [118.9(2)°] bond angles, further confirm the **L^L** structural assignment and help rule out the formation of a hydrogenated variant. The N1–C1–C27–N2 (122.23°) torsion angle indicates a break in conjugation between the two phenanthridine units.

Mixing a CH_2Cl_2 solution of **L^L** with an acetonitrile solution of $Fe(OTf)_2$ produced a deep green product (Fig. 4a). Note: it is important to keep the reaction mixture in the dark to avoid premature product decomposition. Multinuclear NMR spectroscopy and single crystal X-ray diffraction analysis of crystals grown *via* slow mixing of a layer of diethyl ether with a concentrated acetonitrile solution at −25 °C revealed the formation of a pseudo-octahedral Fe(II) complex with the imine and phosphine arms of **L^L** occupying equatorial positions, two acetonitrile units bound axially, and two outer-sphere trifluoromethanesulfonate (triflate) counterions (Fig. 4b). To relieve the steric clashing between C_3–*H* and C_{29}–*H*, the coordinated ligand bends such that the phenanthridinyl units lie at a 35° angle. This steric clashing is the likely origin of the limited photostability of this compound (*vide infra*).

To gain insight into the electronic structure of the complex, a UV-vis absorption spectrum in acetonitrile was collected and TD-DFT calculations were performed on the optimized solution-state geometry. An overlay of the experimental and TD-DFT simulated spectra is shown in Fig. 5, with the absorption spectrum in units of molar extinction coefficients shown in Fig. S2. The absorption spectrum shows multiple overlapping bands in the UV region, a strong absorption feature at 420 nm with a broad tail extending up to 500 nm, and a broad absorption centered at 600 nm. TD-DFT computed vertical excitations reveal that the broad lowest energy absorption band at 600 nm (ε = 1600 M^{-1} cm^{-1}) has metal-to-ligand charge transfer (MLCT) character, with electron density transiting from an Fe localized t_{2g}-type orbital to the vacant, localized C═N π^* orbitals of both phenanthridinyl units of the ligand, consistent with general acceptor character of phenanthridine-based ligands.[21] The higher energy transitions at 420–460 nm (ε ~7000 M^{-1} cm^{-1}) present partial MLCT character with significant contributions from **L^L** localized, intra-ligand charge-transfer (ILCT) character. As we progress into the UV region, metal contribution to the vertical excitations decreases and the transitions are predominantly ILCT. Compound **1** is light sen-

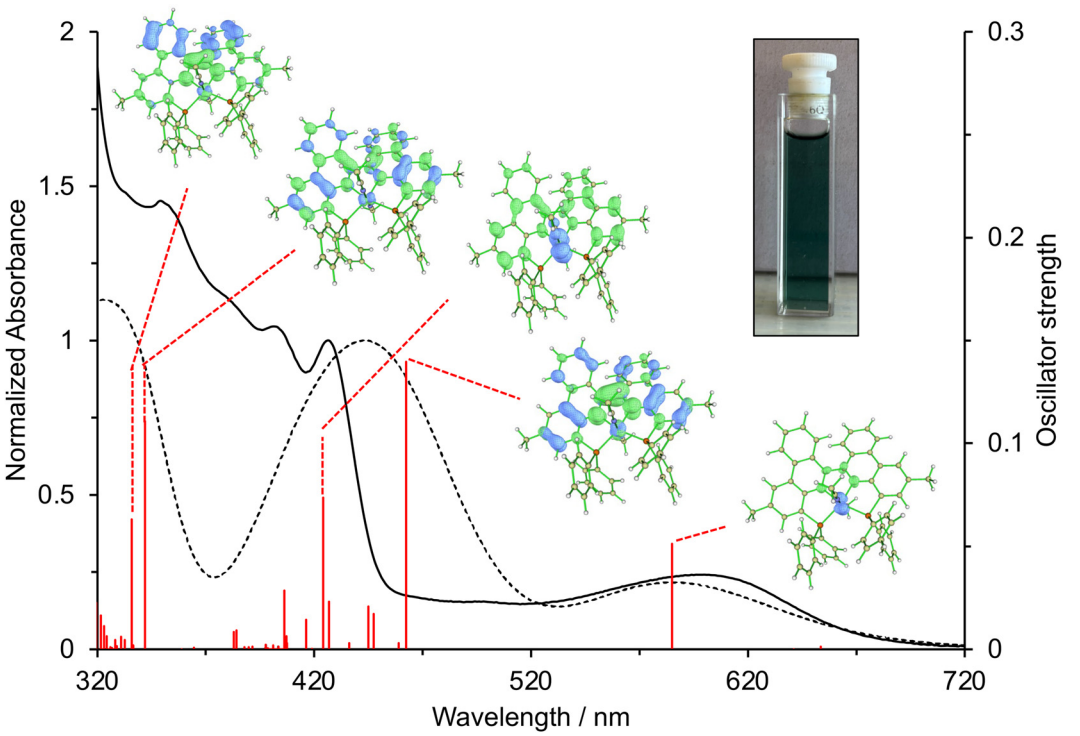

Fig. 5 Experimental UV-vis absorption spectrum (solid black trace) of **1** compared with its TD-DFT simulated spectrum (dashed black trace) and computed vertical energy transitions (solid red lines) in acetonitrile (M06L-RIJCOSX-ZORA-SMD-SARC/J//ZORA-def2-TZVP; FWHM = 0.37 eV), with the inset showing the green colour of the solution. Only the transitions with oscillator strengths >0.001 are shown. Electron–hole density maps are shown for major transitions with relatively high oscillator strengths (isosurface value = 0.002, green = electron density distribution, blue = hole density distribution).

This journal is © The Royal Society of Chemistry 2025

Open Access Article. Published on 30 October 2025. Downloaded on 5/16/2026 7:15:46 PM.
This article is licensed under a Creative Commons Attribution 3.0 Unported Licence.

sitive and slowly degrades over days when consistently exposed to visible light but is stable when stored in the dark, even in air-saturated solutions (see Fig. S3 for details).

Cyclic voltammograms of **1** show two reversible reduction events at −1.04 V and −1.33 V, as well as an irreversible reduction at −2.15 V *vs.* ferrocene/ferrocenium ($FcH^{0/+}$). We attribute the first reduction event to the Fe^{II}/Fe^{I} redox couple. The second reduction likely corresponds to the Fe^{I}/Fe^{0} redox couple, with the possibility of ligand participation. Reduced metal complexes of electron-deficient bipyridine-based ligands have been seen to present ligand-reduced character.[38] Based on previously studied complexes of the monomeric ligand **L**[29] and related phenanthridine-containing ligands,[39,40] we assign the irreversible reduction at much more negative potentials to a wholly ligand-centered reduction. On the oxidative side, the Fe^{III}/Fe^{II} redox couple at −0.35 V and another quasi-reversible oxidation at 0.99 V are also observed. Cyclic voltammograms in the presence of trifluoroacetic acid (TFA) show a current enhancement at the second reduction event (−1.33 V). Both the irreversibility of the anodic wave and the cathodic current response grow with increasing concentration of acid, typical of a catalytic wave. In comparison, there are no changes to the first reduction event (Fig. S4). The direct reduction of trifluoroacetic acid on glassy carbon electrodes is known to occur at −1.81 V *vs.* $FcH^{0/+}$.[41] The current enhancement observed here can therefore be attributed to catalytic hydrogen evolution by **1**.

Since the axial ligand positions in **1** are occupied by what we assume to be labile acetonitrile solvent molecules, these coordination sites can likely be made available for the binding of substrates such as H^+. The mechanism of catalytic HER by transition metal complexes generally involves formation of metal-hydride intermediates.[14] M–H formation can occur *via* one-electron reduction of the catalyst followed by protonation, or *via* two-electron reduction and protonation. H_2 evolution can then either occur homolytically, involving two [M–H] equivalents, or a two-electron reduced M–H complex could be protonated to yield dihydrogen *via* a heterolytic mechanism. In the case of **1**, since HER-associated current enhancement is only observed at the second reduction event, we assign the one-electron reduced species (labelled as $[\mathbf{Fe}]^+$ in Scheme 1) as the catalytically active species. Return anodic scans following the electrocatalytic wave show that, in the presence of acid, the second reduction is irreversible. As the anodic wave for the first reduction ($Fe^{II/I}$ couple) is still observable in the presence of acid (Fig. S4), the first reduction is not accompanied by protonation. The $[Fe]^+$ species may not be nucleophilic enough to be protonated. We therefore propose that, under electrocatalytic conditions, the dicationic Fe(II) complex undergoes sequential one-electron reductions followed by protonation to form an $[Fe–H]^+$ species, with a hydride occupying the place of an axial acetonitrile molecule (Scheme 1). Subsequent protonation then yields H_2 and regenerates the dicationic Fe(II) species, likely stabilized by recoordination of solvent unit to saturate the metal's coordination sphere.

Considering the observed HER might originate from deposition of a catalytically active species on the surface of the electrode rather than from homogeneous **1**, we subjected a solution of **1** to 50 cycles of electrocatalysis scanning from −0.1 to

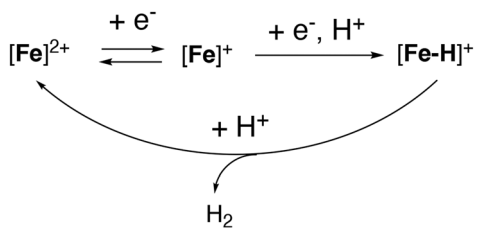

Scheme 1 Proposed heterolytic pathway for the reduction of protons from **1** *via in situ* generated $[Fe]^+$.

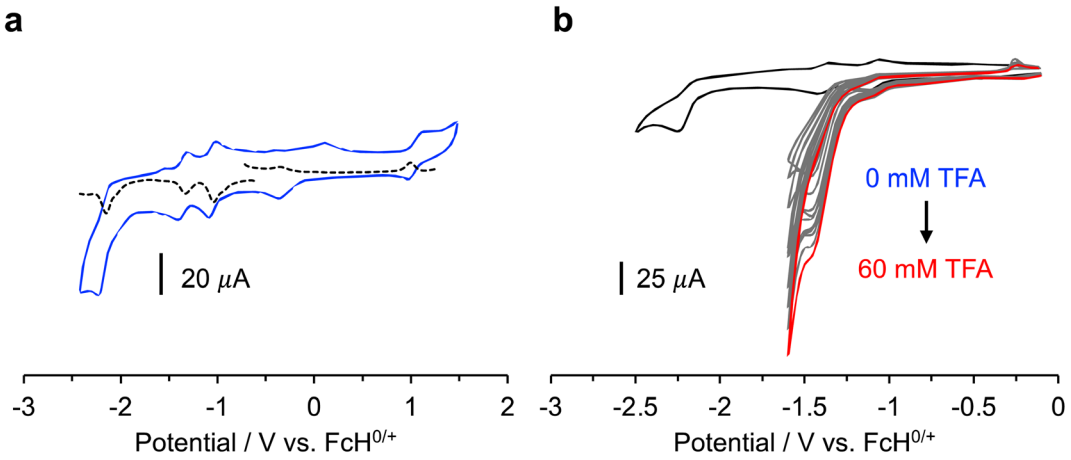

Fig. 6 (a) Cyclic voltammogram (solid blue trace) and differential pulse voltammogram (DPV, dashed black trace) of a 1 mM solution of **1** in acetonitrile containing 0.1 M nBu$_4$NPF$_6$ as the supporting electrolyte, collected using a glassy carbon working electrode, Pt wire reference electrode, and Ag/Ag^+ pseudo-reference electrode. (b) Reductive side of the cyclic voltammogram of a 1 mM solution of **1** collected in the presence of varying concentrations of trifluoroacetic acid. Concentrations of TFA were varied in increments of 4 mM, with the blue trace corresponding to 0 M and the red trace corresponding to 60 mM TFA.

Open Access Article. Published on 30 October 2025. Downloaded on 5/16/2026 7:15:46 PM.
This article is licensed under a Creative Commons Attribution 3.0 Unported Licence.

−1.7 V *vs.* $FcH^{0/+}$. Removing the electrode to a fresh solution of electrolyte and acid which did not contain added **1**, we do not see features in subsequent CV cycles consistent with electrocatalysis (Fig. S5). This confirmed that no electrocatalytically active material deposits on the electrode after at least 50 cycles of electrocatalysis, indicating that compound **1** behaves as the true homogeneous catalyst.

Using the half-wave potential of the catalytic wave observed under HER conditions (−1.37 V) and taking −0.779 V as the thermodynamic potential for the reduction of TFA in acetonitrile,[41] we estimate an overpotential of 591 mV (see SI for the calculation). To determine the order of the reaction with respect to acid, i_c/i_p was plotted *versus* the concentration of acid with i_c corresponding to the peak current of the catalytic wave and i_p the current of the wave in the absence of substrate. Fig. 6b shows that the peak current increases with increasing concentration of acid. Fig. 7a reveals a linear relationship between i_c/i_p and the concentration of acid, with an R^2 value of 0.96. The catalytic reaction is thus second-order with respect to acid, with a maximum i_c/i_p observed of 13.6. The order of the reaction with respect to the catalyst concentration can also be determined by plotting peak current *vs.* catalyst concentration (Fig. 7b). The linear relationship observed between peak current and concentration of the electrocatalyst shows a first-order reaction respect to **1**. This is consistent with the proposed heterolytic pathway for H_2 generation.

From Fig. 6b, it is evident that even at high substrate concentrations, a catalytic plateau current is not achieved and the S-shaped curve that is expected for a catalytic reaction that is not limited by the diffusion of the substrate is not obtained. This is indicative of competing side phenomenon such as substrate consumption, catalyst deactivation, or product inhibition.[42] In such cases, foot-of-the-wave analysis (FOWA) can be used to gain insights on the turnover frequency (TOF) and k_{obs} of the reaction by focusing our analysis on the foot of the

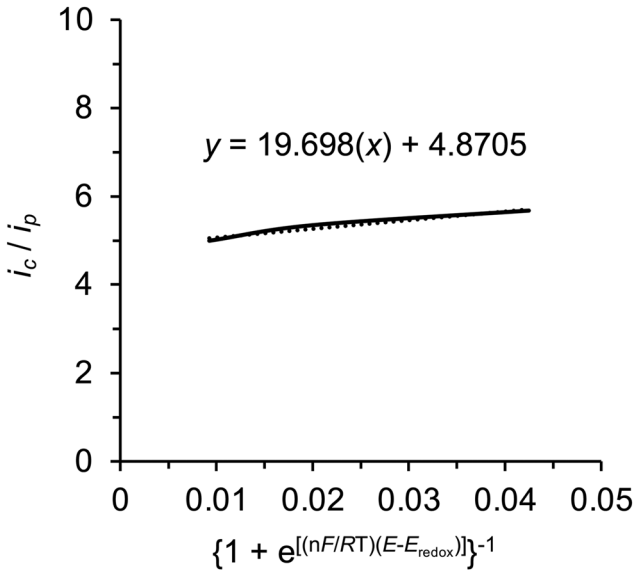

Fig. 8 Linear fit obtained for FOWA analysis for **1** between −1.25 V and −1.33 V *vs.* $FcH^{0/+}$.

catalytic wave; *i.e.*, the initial portion of the wave where the CV response is linear and it can be assumed that competing side phenomenon are not occurring.[43,44] The following equation can then be used to estimate the observed rate constant:

$$\frac{i_c}{i_p} = \frac{2.24\sqrt{\frac{RT}{nFv}}\sqrt{n'k_{obs}}}{1 + \exp\left[\frac{nF}{RT}(E - E_{redox})\right]}$$

where i_c is the current of the catalytic wave, i_p is the current of that wave in the absence of an added substrate, R is the gas constant in J mol^{-1} K^{-1}, T is the temperature in K, F is the

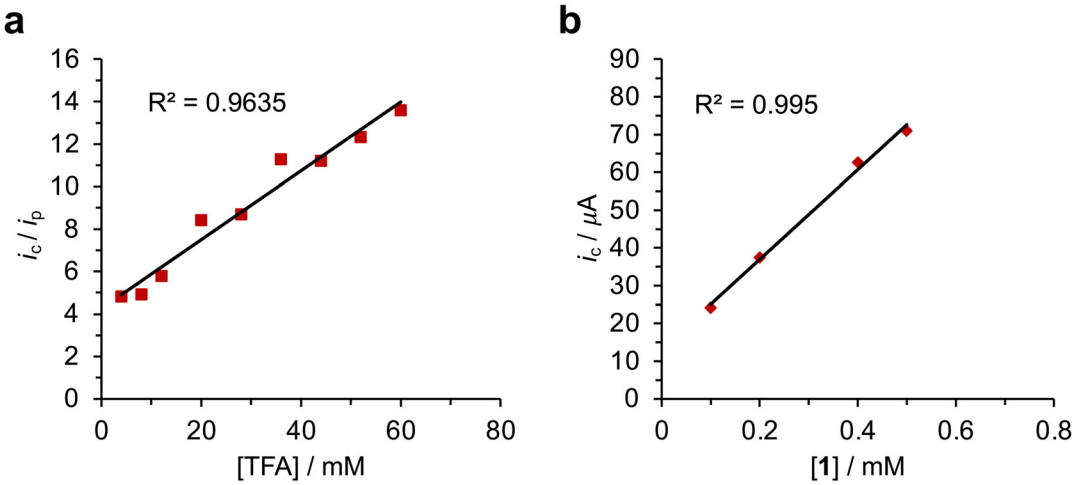

Fig. 7 (a) Plot of i_c/i_p *vs.* the concentration of TFA, obtained from CVs of a 1 mM solution of **1** in CH_3CN with 0.1 M nBu_4NPF_6 as supporting electrolyte and varying amounts of acid. (b) Plot of peak current *vs.* the concentration of **1**, obtained from cyclic voltammograms of a 2 mM solution of TFA in CH_3CN, with 0.1 M nBu_4NPF_6 as supporting electrolyte and varying amounts of **1**. All CVs were collected at a scan rate of 0.1 V s^{-1}.

This journal is © The Royal Society of Chemistry 2025

Open Access Article. Published on 30 October 2025. Downloaded on 5/16/2026 7:15:46 PM.
This article is licensed under a Creative Commons Attribution 3.0 Unported Licence.

Table 1 Comparison of the electrocatalytic activity of **1** with related Fe complexes

Compound	Structure	Overpotential (η)/mV	k_{obs}/s^{-1}	Ref.
A	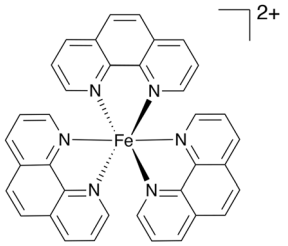	838	0.175	45
B	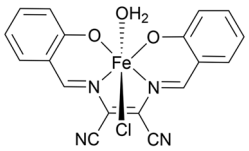	830	0.224	46
C	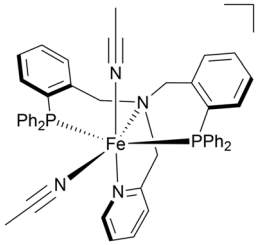	487	29	47
D	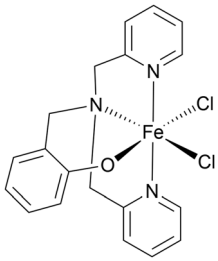	800	3000	18
E	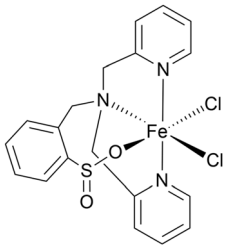	800	3300	48
F	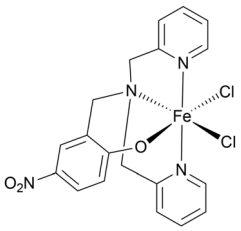	300	550	49
1	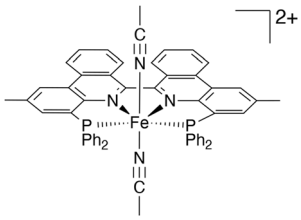	591	602	This work

Open Access Article. Published on 30 October 2025. Downloaded on 5/16/2026 7:15:46 PM. This article is licensed under a Creative Commons Attribution 3.0 Unported Licence.

Faraday constant in C mol^{-1}, ν is the scan rate in V s^{-1}, E is the potential in V, E_{redox} is the potential where catalysis occurs in V, n is the number of electrons transferred at the electrode in the catalytic process, and n' is the number of equivalents of catalyst required for turnover. In our case, catalysis involves sequential two-electron reductions of the Fe(II) species **1**. Accordingly, we determine the number of electrons transferred from the electrode that are involved in generating the catalytic current to be $n = 2$. Since HER seems to be occurring through a heterolytic pathway with one equivalent of complex necessary for turnover, $n' = 1$. E_{redox}, the potential at which catalysis takes place, is taken as the half-wave potential of the catalytic wave, at the point where the current is half of the maximum peak current (−1.37 V *vs.* $FcH^{0/+}$). Using the CV obtained in the presence of 60 mM TFA and incorporating these values in the above equation, FOWA was performed and $\frac{i_c}{i_p}$ was plotted *versus* $\frac{1}{1+\exp\left[\frac{nF}{RT}(E-E_{redox})\right]}$ for the linear region near the foot of the catalytic wave. That is, at potentials ranging between −1.25 V and −1.33 V. Assuming no competing side phenomenon occurring at the foot of the wave, this plot should yield a straight line with a slope equal to $2.24\sqrt{\frac{RT}{nFv}}\sqrt{n'k_{obs}}$. It is worth highlighting that in our case, we still expect there to be slight deviations from the ideal scenario for FOWA because we have a redox event (the $Fe^{II/I}$ couple) occurring near the foot of the catalytic wave, which could give some diffusional contributions to the current observed at the foot of the wave. Nevertheless, FOWA should still give us an estimate of the rate constant with which catalytic HER occurs. Fig. 8 shows the plot obtained, with a slope of 19.698. Using the relationship $m = 2.24\sqrt{\frac{RT}{nFv}}\sqrt{n'k_{obs}}$, k_{obs} is calculated at 602 s^{-1}.

Comparing this to related Fe(II) and Fe(III) complexes shown in Table 1, complex **1** operates at a lower overpotential than a recently reported Fe(II) complex of phenanthroline (**A**)[45] and an Fe(III) complex of a tetradentate Schiff base ligand (**B**),[46] but has a slightly higher overpotential than the closely related Fe(II) complex **C** with a tetradentate N_2P_2 ligand.[47] Complex **1** does however show a significantly improved k_{obs} compared with all three of **A**–**C**. Some of the most active Fe(III)$NNOCl_2$ HER catalysts (complexes **D**–**F**) have overpotentials ranging between 300–800 mV and k_{obs} of 550–3300 s^{-1}.[18,48,49] Complex **1** seems to be approaching the activity of these species. This showcases the potential of π-extended tetradentate P^N-based ligands for boosting the electrocatalytic activity of Fe(II) for homogeneous HER and opens up the possibility of deploying benzannulated multidentate ligands in homogeneous HER electrocatalysis more widely.

Conclusions

In summary, we have shown how a substituted 6,6′-biphenanthridine (biphe) can be selectively formed from its monomer *via* reductive dimerization using sodium as the reducing agent. This protocol gives access to a tetradentate benzannulated P^N^N^P ligand **L^L** with two phosphine donor arms, extending the binding ability of biphe.[22,23] This ligand can bind to Fe(II), forming a pseudo-octahedral Fe(II) complex (**1**) that presents two accessible, reversible reduction events, highlighting the molecule's ability to store electrons. The two-electron reduced complex can efficiently catalyze the reduction of protons in an acetonitrile solution at a low overpotential of 591 mV and with moderately high k_{obs} of 602 s^{-1}. This corresponds to a high electrocatalytic activity, approaching the efficiency of some of the most active Fe(III) homogeneous HER electrocatalysts. Analysis of the electrochemical behavior shows the HER process to be first-order with respect to the catalyst and second-order with respect to the acid, indicating a heterolytic pathway. We ascribe the high activity of this electrocatalyst to the stabilization of the reduced complex by increased π-extension of the ligand. Given the low photostability of this complex, efforts to planarize the substituted biphe are currently underway, with the goal of eliminating ligand photodissociation and catalyst degradation.

Author contributions

The manuscript was written through contributions of all authors. All authors have given approval to the final version of the manuscript.

Conflicts of interest

There are no conflicts to declare.

Data availability

Supplementary information (SI): multi-nuclear NMR and HR-MS spectra of all new compounds and other supporting data and figures, as well as crystallographic information files containing all X-ray data. See DOI: https://doi.org/10.1039/d5dt02202a.

CCDC 2487856 and 2487857 contain the supplementary crystallographic data for this paper.[50a,b]

Acknowledgements

The Natural Sciences and Engineering Research Council is thanked for a Discovery Grant to D. E. H. (RGPIN-2022-04501) CGS-D Scholarships to B. K. S. and A. K. Purchase of an X-Ray diffractometer was possible through support of the Canada Foundation for Innovation and Research Manitoba (#32146). The Digital Research Alliance of Canada is thanked for computational support.

 This journal is © The Royal Society of Chemistry 2025

Open Access Article. Published on 30 October 2025. Downloaded on 5/16/2026 7:15:46 PM. This article is licensed under a Creative Commons Attribution 3.0 Unported Licence.

References

1 H. Wang, J. Wen and X. Zhang, Chiral Tridentate Ligands in Transition Metal-Catalyzed Asymmetric Hydrogenation, *Chem. Rev.*, 2021, **121**, 7530–7567.

2 D.-H. Liang, C.-J. Hou, Q. Li, H. Qin, L. Li and X.-P. Hu, Chiral P,N,N-Ligands for Asymmetric Hydrogenation, *Adv. Synth. Catal.*, 2024, **366**, 2165–2185.

3 M. P. Carroll and P. J. Guiry, P,N Ligands in Asymmetric Catalysis, *Chem. Soc. Rev.*, 2014, **43**, 819–833.

4 A. Rajmane and A. Kumbhar, Polydentate P,N-Based, Ligands for Palladium-Catalyzed Cross-Coupling Reactions, *Mol. Catal.*, 2022, **532**, 112699.

5 J. Bae and E. J. Cho, P,N Ligand in Ni-Catalyzed Cross-Coupling Reactions: A Promising Tool for π-Functionalization, *ACS Catal.*, 2023, **13**, 13540–13560.

6 L. S. Merz, J. Ballmann and L. H. Gade, Phosphines and N-Heterocycles Joining Forces: An Emerging Structural Motif in PNP-Pincer Chemistry, *Eur. J. Inorg. Chem.*, 2020, **2020**, 2023–2042.

7 A. Mezzetti, Ruthenium Complexes with Chiral Tetradentate PNNP Ligands: Asymmetric Catalysis from the Viewpoint of Inorganic Chemistry, *Dalton Trans.*, 2010, **39**, 7851–7869.

8 W. Zuo, A. J. Lough, Y. F. Li and R. H. Morris, Amine (Imine)Diphosphine Iron Catalysts for Asymmetric Transfer Hydrogenation of Ketones and Imines, *Science*, 2013, **342**, 1080–1083.

9 R. H. Morris, Exploiting Metal–Ligand Bifunctional Reactions in the Design of Iron Asymmetric Hydrogenation Catalysts, *Acc. Chem. Res.*, 2015, **48**, 1494–1502.

10 E. S. Wiedner, A. M. Appel, S. Raugei, W. J. Shaw and R. M. Bullock, Molecular Catalysts with Diphosphine Ligands Containing Pendant Amines, *Chem. Rev.*, 2022, **122**, 12427–12474.

11 A. S. Nanuwa, M. D. Hoffman, K. Nandi and J. M. Blacquiere, Selectivity of Ru and Fe PR2NR'2 Catalysts Toward Acceptorless Dehydrogenation of Benzylamine, *Organometallics*, 2024, **43**, 2342–2348.

12 E. S. Isbrandt, D. E. Chapple, N. T. P. Tu, V. Dimakos, A. M. M. Beardall, P. D. Boyle, C. N. Rowley, J. M. Blacquiere and S. G. Newman, Controlling Reactivity and Selectivity in the Mizoroki–Heck Reaction: High Throughput Evaluation of 1,5-Diaza-3,7-Diphosphacyclooctane Ligands, *J. Am. Chem. Soc.*, 2024, **146**, 5650–5660.

13 H. Land, M. Senger, G. Berggren and S. T. Stripp, Current State of [FeFe]-Hydrogenase Research: Biodiversity and Spectroscopic Investigations, *ACS Catal.*, 2020, **10**, 7069–7086.

14 L. Tong, L. Duan, A. Zhou and R. P. Thummel, First-Row Transition Metal Polypyridine Complexes That Catalyze Proton to Hydrogen Reduction, *Coord. Chem. Rev.*, 2020, **402**, 213079.

15 I. Bhugun, D. Lexa and J.-M. Savéant, Homogeneous Catalysis of Electrochemical Hydrogen Evolution by Iron(0) Porphyrins, *J. Am. Chem. Soc.*, 1996, **118**, 3982–3983.

16 L.-L. Zhou, L.-Z. Tang, Y.-X. Zhang and S.-Z. Zhan, Synthesis of a Molecular Electrocatalyst Based on an Iron (III) Complex Supported by Amine-Bis(Phenolate) Ligand for Water Reduction, *Polyhedron*, 2015, **92**, 124–129.

17 M. J. Rose, H. B. Gray and J. R. Winkler, Hydrogen Generation Catalyzed by Fluorinated Diglyoxime–Iron Complexes at Low Overpotentials, *J. Am. Chem. Soc.*, 2012, **134**, 8310–8313.

18 G. P. Connor, K. J. Mayer, C. S. Tribble and W. R. McNamara, Hydrogen Evolution Catalyzed by an Iron Polypyridyl Complex in Aqueous Solutions, *Inorg. Chem.*, 2014, **53**, 5408–5410.

19 A. Call, Z. Codolà, F. Acuña-Parés and J. Lloret-Fillol, Photo- and Electrocatalytic H2 Production by New First-Row Transition-Metal Complexes Based on an Aminopyridine Pentadentate Ligand, *Chem. – Eur. J.*, 2014, **20**, 6171–6183.

20 N. A. C. dos Santos, M. Natali, E. Badetti, K. Wurst, G. Licini and C. Zonta, Cobalt, Nickel, and Iron Complexes of 8-Hydroxyquinoline-Di(2-Picolyl)Amine for Light-Driven Hydrogen Evolution, *Dalton Trans.*, 2017, **46**, 16455–16464.

21 D. E. Herbert, When Is a Pyridine Not a Pyridine? Benzannulated N-Heterocyclic Ligands in Molecular Materials Chemistry, *Can. J. Chem.*, 2023, **101**, 892–902.

22 D. B. Nemez, I. B. Lozada, J. D. Braun, J. A. G. Williams and D. E. Herbert, Synthesis and Coordination Chemistry of a Benzannulated Bipyridine: 6,6′-Biphenanthridine, *Inorg. Chem.*, 2022, **61**, 13386–13398.

23 D. B. Nemez, R. J. Ortiz, K. A. Veilleux, J. A. G. Williams and D. E. Herbert, In Pursuit of Low Energy Phosphorescence: Late Metal Coordination Complexes of the Planar, π-Extended Bipyridyl Ligand 6,6′,7,7′-Biphenanthridine, *Chem. – Eur. J.*, 2025, e01802.

24 R. Mondal, P. K. Giesbrecht and D. E. Herbert, Nickel(II), Copper(I) and Zinc(II) Complexes Supported by a (4-Diphenylphosphino)Phenanthridine Ligand, *Polyhedron*, 2016, **108**, 156–162.

25 M. Drosou, F. Kamatsos and C. A. Mitsopoulou, Recent Advances in the Mechanisms of the Hydrogen Evolution Reaction by Non-Innocent Sulfur-Coordinating Metal Complexes, *Inorg. Chem. Front.*, 2020, **7**, 37–71.

26 P. Mandapati, P. K. Giesbrecht, R. L. Davis and D. E. Herbert, Phenanthridine-Containing Pincer-like Amido Complexes of Nickel, Palladium, and Platinum, *Inorg. Chem.*, 2017, **56**, 3674–3685.

27 R. Mondal, I. B. Lozada, R. L. Davis, J. A. G. Williams and D. E. Herbert, Site-Selective Benzannulation of N-Heterocycles in Bidentate Ligands Leads to Blue-Shifted Emission from [(P^N)Cu]2(μ-X)2 Dimers, *Inorg. Chem.*, 2018, **57**, 4966–4978.

28 R. Mondal, I. B. Lozada, R. L. Davis, J. A. G. Williams and D. E. Herbert, Exploiting Synergy between Ligand Design and Counterion Interactions to Boost Room Temperature Phosphorescence from Cu(I) Compounds, *J. Mater. Chem. C*, 2019, **7**, 3772–3778.

Open Access Article. Published on 30 October 2025. Downloaded on 5/16/2026 7:15:46 PM. This article is licensed under a Creative Commons Attribution 3.0 Unported Licence.

29 R. Mondal, J. D. Braun, I. B. Lozada, R. Nickel, J. van Lierop and D. E. Herbert, Group VIII Coordination Complexes of Bidentate P^N Ligands Bearing π-Extended Quinoline or Phenanthridine N-Heterocycles, *New J. Chem.*, 2021, **45**, 4427–4436.
30 R. Mondal and D. E. Herbert, Synthesis of Pyridines, Quinolines, and Pyrimidines via Acceptorless Dehydrogenative Coupling Catalyzed by a Simple Bidentate P^N Ligand Supported Ru Complex, *Organometallics*, 2020, **39**, 1310–1317.
31 R. Mondal, I. B. Lozada, O. Stotska and D. E. Herbert, Catalytic Synthesis of Luminescent Pyrimidines via Acceptor-Less Dehydrogenative Coupling, *J. Org. Chem.*, 2020, **85**, 13747–13756.
32 R. Mondal, J. D. Braun, B. K. Sidhu, D. E. Nevonen, V. N. Nemykin and D. E. Herbert, Catalytic Synthesis of Donor-Acceptor-Donor (D-A-D) and Donor-Acceptor-Acceptor (D-A-A) Pyrimidine-Ferrocenes via Acceptorless Dehydrogenative Coupling: Synthesis, Structures, and Electronic Communication, *Organometallics*, 2021, **40**, 1765–1775.
33 B. K. Sidhu, R. Mondal and D. E. Herbert, Tandem Hydrogen-Borrowing Dehydrogenative Coupling and Hydrodefluorination, *Adv. Synth. Catal.*, 2024, **366**(8), 1809–1819.
34 P. K. Giesbrecht, D. B. Nemez and D. E. Herbert, Electrochemical Hydrogenation of a Benzannulated Pyridine to a Dihydropyridine in Acidic Solution, *Chem. Commun.*, 2018, **54**, 338–341.
35 E. Garcia-Torres and D. E. Herbert, Electrochemical Hydrogenation of N-Heterocycles and Related Substrates: A Mini-Review, *Electrochem. Sci. Adv.*, 2025, **5**, e00019.
36 J. J. Eisch and R. M. Thompson, Chemistry of Alkali Metal-Unsaturated Hydrocarbon Adducts. II. Radical-Anion Intermediates in the Metal Reductions of Aza-Aromatic Heterocycles, *J. Org. Chem.*, 1962, **27**, 4171–4179.
37 D. D. Tanner and C. M. Yang, On the Structure and Mechanism of Formation of the Lansbury Reagent, Lithium Tetrakis(N-Dihydropyridyl)Aluminate, *J. Org. Chem.*, 1993, **58**, 1840–1846.
38 J. M. Smieja, E. E. Benson, B. Kumar, K. A. Grice, C. S. Seu, A. J. M. Miller, J. M. Mayer and C. P. Kubiak, Kinetic and Structural Studies, Origins of Selectivity, and Interfacial Charge Transfer in the Artificial Photosynthesis of CO, *Proc. Natl. Acad. Sci. U. S. A.*, 2012, **109**, 15646–15650.
39 J. D. Braun, I. B. Lozada, C. Kolodziej, C. Burda, K. M. E. Newman, J. van Lierop, R. L. Davis and D. E. Herbert, Iron(II) Coordination Complexes with Panchromatic Absorption and Nanosecond Charge-Transfer Excited State Lifetimes, *Nat. Chem.*, 2019, **11**, 1144–1150.
40 C. B. Larsen, J. D. Braun, I. B. Lozada, K. Kunnus, E. Biasin, C. Kolodziej, C. Burda, A. A. Cordones, K. J. Gaffney and D. E. Herbert, Reduction of Electron Repulsion in Highly Covalent Fe-Amido Complexes Counteracts the Impact of a Weak Ligand Field on Excited-State Ordering, *J. Am. Chem. Soc.*, 2021, **143**, 20645–20656.
41 B. D. McCarthy, D. J. Martin, E. S. Rountree, A. C. Ullman and J. L. Dempsey, Electrochemical Reduction of Brønsted Acids by Glassy Carbon in Acetonitrile—Implications for Electrocatalytic Hydrogen Evolution, *Inorg. Chem.*, 2014, **53**, 8350–8361.
42 E. S. Rountree, B. D. McCarthy, T. T. Eisenhart and J. L. Dempsey, Evaluation of Homogeneous Electrocatalysts by Cyclic Voltammetry, *Inorg. Chem.*, 2014, **53**, 9983–10002.
43 C. Costentin, S. Drouet, M. Robert and J.-M. Savéant, Turnover Numbers, Turnover Frequencies, and, Overpotential in Molecular Catalysis of Electrochemical Reactions. Cyclic Voltammetry and Preparative-Scale Electrolysis, *J. Am. Chem. Soc.*, 2012, **134**, 11235–11242.
44 C. Costentin and J.-M. Savéant, Multielectron, Multistep Molecular Catalysis of Electrochemical Reactions: Benchmarking of Homogeneous Catalysts, *ChemElectroChem*, 2014, **1**, 1226–1236.
45 S.-P. Luo, Q.-X. Peng, J. Liu and S.-Z. Zhan, Effect of Metal Centers on Electrocatalytic Hydrogen Generation Catalyzed by Coordinatively Saturated Metal-1,10-Phenanthroline Complexes, *Polyhedron*, 2018, **139**, 44–49.
46 L.-Z. Fu, L.-L. Zhou and S.-Z. Zhan, Electrochemical-Driven Water Reduction and Oxidation Catalyzed by an Iron(III) Complex Supported by 2,3-Bis(2-Hydroxybenzylideneimino)-2,3-Butenedinitrile, *RSC Adv.*, 2015, **5**, 42287–42293.
47 D. Huang, B. He, Y. Zhao, M. Liu and L. Wang, Homogeneous Electrocatalytic Hydrogen Evolution by a N2P2Fe(II) Complex: Structural Characterization of Iron-Hydride Intermediate, *J. Mol. Struct.*, 2025, **1325**, 141021.
48 A. C. Cavell, C. L. Hartley, D. Liu, C. S. Tribble and W. R. McNamara, Sulfinato Iron(III) Complex for Electrocatalytic Proton Reduction, *Inorg. Chem.*, 2015, **54**, 3325–3330.
49 C. L. Hartley, R. J. DiRisio, T. Y. Chang, W. Zhang and W. R. McNamara, Electrocatalytic Hydrogen Evolution by an Iron Complex Containing a Nitro-Functionalized Polypyridyl Ligand, *Polyhedron*, 2016, **114**, 133–137.
50 (*a*) CCDC 2487856: Experimental Crystal Structure Determination, 2025, DOI: 10.5517/ccdc.csd.cc2phtfg; (*b*) CCDC 2487857: Experimental Crystal Structure Determination, 2025, DOI: 10.5517/ccdc.csd.cc2phtgh.

This journal is © The Royal Society of Chemistry 2025